The Kinetics and Mechanism of Pyrite Thermal Decomposition

Y. Hong and B. Fegley Jr.

Planetary Chemistry Laboratory, Department of Earth and Planetary Sciences, Campus Box 1169, Washington University, One Brookings Drive, St. Louis, Missouri 63130-4899, USA

Key Words: Chemical Kinetics / Gases / Reaction Mechanism / Spectroscopy, X-ray / Thermodynamics

Pyrite (FeS_2) decomposition in He, N_2, CO_2-CO-SO_2, O_2-CO_2 and H_2S-H_2 gas mixtures was studied from 400–590 °C using optical microscopy, X-ray diffraction, electron microprobe analyses, and gas chromatography. The rate constants were determined from the weight loss and the thickness change of pyrite in reacted samples. The temperature dependent composition of the product, pyrrhotite ($Fe_{1-x}S$), was measured by electron microprobe analysis and X-ray diffraction. Pyrite decomposition to pyrrhotite and sulfur vapor (dominantly S_2) was observed in all gases and follows linear kinetics. The apparent activation energy of pyrite thermal decomposition is 297 ± 34 kJ mol^{-1} in inert gases (e.g. He, N_2), and 275 ± 20 kJ mol^{-1} in purified CO_2 and in low concentration CO-SO_2 gas mixtures with CO_2. The rate constants are the same regardless of gas composition at a given temperature. In oxidizing (O_2-CO_2) or reducing (H_2S-H_2) gas mixtures, the rate constants are larger than that in inert gases because additional reactions between pyrite and oxidizing/reducing gases accelerate the overall process while reducing the apparent activation energies. A mechanism of pyrite decomposition, which explains our experimental results, as well as the discordant activation energy data in the literature, is proposed.

1. Introduction

The thermal decomposition of pyrite (FeS_2) to pyrrhotite ($Fe_{1-x}S$) and sulfur vapor (S_2)

$$(1-x)FeS_2 = Fe_{1-x}S + (0.5-x)S_2(g) \quad (1)$$

is an important chemical reaction for technological applications such as coal conversion [1], ceramic manufacture from pyrite-bearing clays [2], sulfur and sulfuric acid manufacturing [3, 4], and gold extraction by sulfide ore roasting [5]. It is also an important geochemical process in terrestrial geochemistry [6], in the geochemistry of the planet Venus [7], and in the geochemistry of Io, the innermost Galilean satellite of Jupiter [8].

Pyrite thermal decomposition has been studied by a number of investigators [1, 2, 5, 9–22], however, discordant results for the rate and activation energy have been reported in the literature (as shown in Table 1, the reported activation energy ranges from 110 to 310 kJ/mol). In this work we report a comprehensive study that combines thermodynamic calculations with kinetic studies and analytical data on gases and solids, in order to provide a better understanding of the kinetics and mechanism of pyrite thermal decomposition, and to evaluate the differences in the experimental data in the literature. Elsewhere we discuss the application of our results to sulfur geochemistry of Earth, Venus, and Io.

2. Experimental

2.1 Materials and Characterization

Pyrite from Zacatecas, Mexico and Huanzala, Peru were purchased from Ward's Natural Science Co. (Rochester, NY). Reflected light microscopy of several samples did not show any other phases. The XRD patterns are identical to that of a pyrite standard (JCPDS pattern 42-1340). Electron microprobe analyses showed 46.16 ± 0.80% Fe and 53.32 ± 0.68% S (mean of 19 analyses with 2σ errors) in good agreement with the values of 46.55% Fe and 53.45% S for stoichiometric pyrite. Gravimetric analyses by quantitative combustion of pyrite to hematite (Fe_2O_3) gave S/Fe atomic ratios of 2.001 ± 0.001 (2σ) and 2.000 ± 0.001 (2σ) for the Mexican and Peruvian pyrite, respectively. Density measurements on carefully weighed and measured regular pieces gave 4.92 g cm^{-3} for Peruvian pyrite, and 4.89 g cm^{-3} for Mexican pyrite, in agreement with values of 4.89–5.03 g cm^{-3} listed for pure pyrite by Deer et al. [23]. These analyses show that the pyrite samples are pure, stoichiometric FeS_2.

The pyrite samples were cut into slices about $1-2 \times 1 \times 0.05$ cm and polished to 0.25 μm for the kinetic measurements. Prior to reaction, the slices were measured to the nearest 0.00025 cm with a micrometer and weighed to the nearest microgram with an analytical balance. The surface areas measured by N_2 adsorption at liquid nitrogen temperature are close to the geometric surface areas of the pyrite samples.

2.2 Pyrite Decomposition Reactions

Pyrite decomposition was studied in one atmosphere gas mixing vertical tube furnaces (Deltech, Denver, CO). Fig. 1 shows a schematic diagram of our experimental setup. The polished pyrite slices were hung from fine Pt-wires with calibrated Pt/Pt-Rh thermocouples right next to the samples. The samples were first inserted into the brass fittings at the top of the furnaces, where the temperature was ~50 °C. We used gas chromatography to verify that all air was flushed out by the gas flow before we lowered the samples into the isothermal hot zones of ~5 cm, which were set to the reaction temperatures. Typically, a sample reached the run temperature in ~5 min and reaction took place at that temperature under atmospheric pressure in the desired gas mixtures. At end of a run, the slice was raised to the cool top of the furnace, and the sample temperature dropped below 50 °C within 5 min.

  0005-9021/97/1212-1870 $ 17.50+.50/0

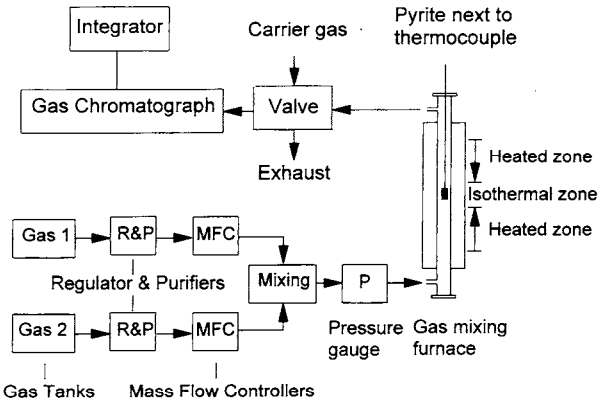

Fig. 1
A schematic diagram of the experimental setup for the pyrite decomposition reactions

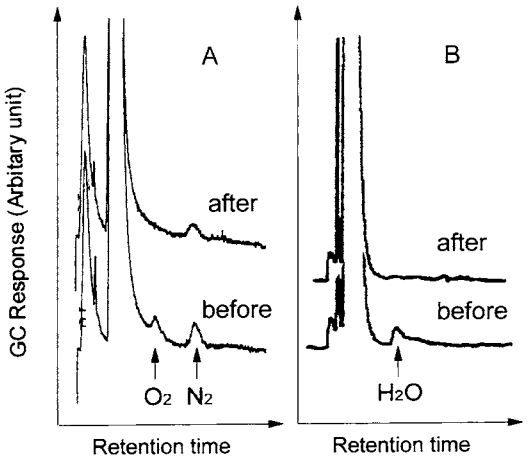

Fig. 2
Gas chromatograms of Coleman grade CO_2 before and after purification to remove O_2 (A) and water vapor (B). (A) Purification done with a 150 cc/min Coleman CO_2 flow passing through a column packed with copper turnings at 250 °C. The analyses were done with a CTR I column in the gas chromatograph. (B) Purification done with a flow of 150 cc/min Coleman CO_2 passing through a $Mg(ClO_4)_2$ column at 25 °C, and analyses were done with a Porapak Q column in the gas chromatograph

2.3 Gas Mixtures

Pyrite decomposition was studied in 11 different gases or gas mixtures: these gases are either inert, reducing or oxidizing. Eight are commercial gases or gas mixtures: Coleman instrument grade CO_2 (99.99%), He (Ultra High Purity grade, 99.999%), N_2 (UHP, 99.999%), 108 ppmv CO (Chemical Purity grade, 99.5%) in CO_2, 1003 ppmv CO (CP, 99.5%) in CO_2, 0.97% SO_2 (Anhydrous grade, 99.98%) in CO_2, 1009 ppmv O_2 (99.98%) in CO_2 and 109 ppmv H_2S (CP, 99.5%) in H_2 (UHP, 99.999%). All CO_2 mixtures are made with Coleman instrument grade CO_2 (99.99%). Concentrations are given in volume% or parts per million by volume (ppmv).

These premixed CO-CO_2, SO_2-CO_2, and O_2-CO_2 gas mixtures were certified standards, accurate to ±5% of the labeled concentration of the minor component. Three other gas mixtures were made by mixing the corresponding pure gas or gas mixtures using calibrated electronic mass flow controllers (Tylan Corp.). They are 54 ppm CO-0.48% SO_2 in Coleman CO_2, and 54 ppm CO in Coleman CO_2, and 100 ppm O_2 in CO_2.

Coleman grade CO_2 contains several parts per million by volume (ppmv) of N_2, O_2, and H_2O impurities. Approximately 2 ppmv O_2 and ~10 ppmv H_2O were detected in a typical Coleman CO_2 cylinder by gas chromatography. This is illustrated in Fig. 2A and B which show chromatograms of CO_2 before purification. By comparison, Fegley et al. [11] measured ≤1 ppmv O_2 in Coleman grade CO_2 using a zirconia-based ceramic oxygen fugacity sensor. Fegley and Prinn [24] reported <1 ppmv O_2 and ≤10 ppmv H_2O in the Coleman grade CO_2 and CO_2 gas mixtures used in their experiments. These analyses were done by the commercial supplier.

The oxygen and H_2O impurities in the gas were removed in our experiments by passing them through hot copper turnings at 250 – 300 °C and magnesium perchlorate. Fig. 2A and B show that no H_2O or O_2 were observed after purification by gas chromatography at our detection limit (~1 ppm) in CO_2.

2.4 Gas Chromatrography

The components in the gas mixtures and in the gaseous products were indentified and quantified with a Hewlett Packard 5890 Series II Gas Chromatograph. UHP grade He was used as carrier gas, and it was further purified with a He purifier (Alltech Co.). Analyses of CO_2, O_2-CO_2, CO-CO_2, SO_2-CO-CO_2 were done with a Porapak Q column at 60 °C and a carrier gas flow rate of 100 ml min^{-1}. A CTR I Column (Alltech Co.) at 35 °C was used specifically to separate O_2 from N_2 and CO in the gas mixtures. Gas lines connected the furnace exhausts to an automated gas sampling valve on the gas chromatograph, and loop sizes of 1.0 or 0.25 ml were used on the gas sampling valve.

2.5 Characterization of Reacted Samples

2.5.1 X-Ray Diffraction

XRD patterns of the starting materials and reaction products were obtained using a Rigaku vertical powder diffractometer with Cu Kα radiation (λ = 1.540598 Å) and Materials Data Incorporated (MDI) software. A silicon powder standard (NIST 640b) was used to calibrate the diffraction angle. In many cases the XRD patterns of the product layers were taken to identify the phases present, and the d_{102} reflection of pyrrhotite was used to calculate its composition, according to the equation given by Yund and Hall [25]:

$$\text{Atomic\% (Fe in pyrrhotite)} = 45.212 + 72.86\,(d_{102} - 2.0400) + 311.5\,(d_{201} - 2.0400)^2 \quad (2)$$

2.5.2. Reflected Light Microscopy

The microstructures of polished cross sections of the reacted samples were examined by reflected light with an Olympus metallurgical microscope equipped with a Sony video printer and a 35 mm camera. The thickness of the remaining pyrite in the reacted samples was also measured using a calibrated scale. The polished cross sections were prepared by mounting samples in epoxy and polishing them on an automated polishing machine.

2.5.3 Electron Microprobe Analyses

Electron microprobe analyses were done with the Washington University JEOL-733 electron microprobe equipped with Advanced Microbeam automation. An accelerating voltage of 15 kV was used with 30 nA beam current and a beam diameter of 1 μm. X-ray matrix corrections were based on a modified CITZAF routine [11, 26]. Stoichiometric pyrite (Taylor Co.) was used as a primary standard. In some cases, electron microprobe analyses were used to measure pyrrhotite composition in the products.

3. Results

We report general observations and qualitative results, and then kinetics results in this section.

3.1 Iron sulfides

3.1.1 Microphotography

Typical changes in the microstructures and morphologies during pyrite decomposition in CO_2 are shown in Fig. 3. A porous pyrrhotite layer forms on the pyrite (Fig. 3A), and the porous layer grows thicker as the reaction proceeds (Fig. 3B), until all pyrite is decomposed (Fig. 3C). The product pyrrhotite layer is so porous that a fresh pyrite surface is always exposed to the gas flow, and the gaseous products can be easily swept away.

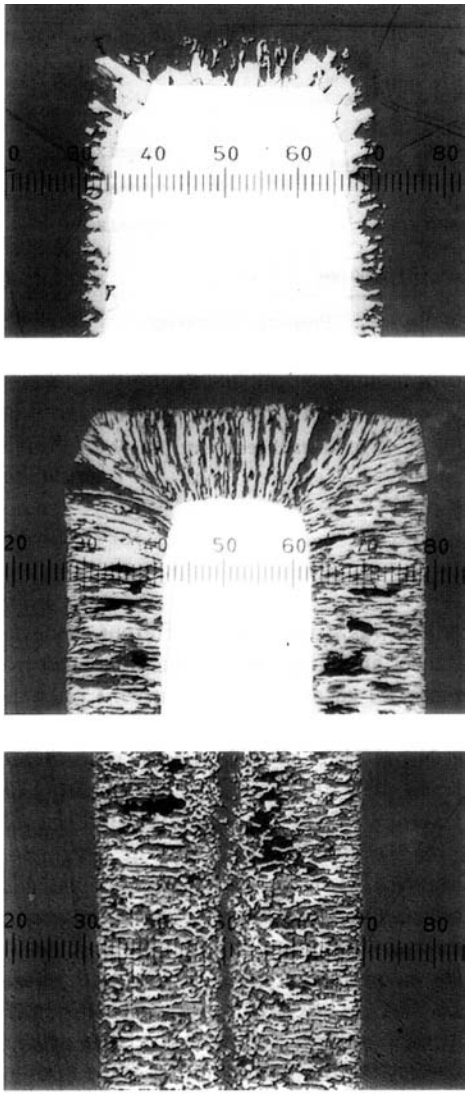

Fig. 3
Reflected light photomicrographs showing the reaction progress. A, B, C correspond to reaction extents of 13.4, 38.8, and 100%, respectively. 10 units in the scale bar = 167 μm

3.1.2 X-Ray Diffraction

In the investigated temperature range, pyrrhotite with a temperature dependent Fe/S ratio was the only phase detected in the run products. In particular, no iron oxides were detected. The Fe content (atomic%) in the pyrrhotite products was determined from the position of the (102) reflection, and is plotted (black dots) on the Fe-S phase diagram shown in Fig. 4. The data are close to the solid line, which is the phase boundary between the single phase pyrrhotite stability field and the two phase pyrite + pyrrhotite field given by Stolen and Gronvold [27]. At the temperatures we used, the pyrrhotites have a composition close to $Fe_{0.875}S$, or Fe_7S_8.

3.1.3 Electron Microprobe Analysis

Some of the pyrrhotites were also analyzed by electron microprobe. The measured Fe contents are plotted as the hollow squares on Fig. 4. The XRD and microprobe data are in good agreement with each other, and with the pyrrhotite-pyrite + pyrrhotite phase boundary [27].

3.2 Sulfur-Bearing Gases

3.2.1 Sulfur Vapor

When pyrite decomposition was performed in inert gases, condensed sulfur was observed in the water cooled gas outlet at the top of the furnace, consistent with the net chemical reaction:

$$(1-x)FeS_2 = Fe_{1-x}S + (0.5-x)S_2(g) \quad (1)$$

The sulfur vapor over pyrite is dominantly $S_2(g)$ under our experimental conditions, and the temperature dependence of the sulfur vapor pressure is:

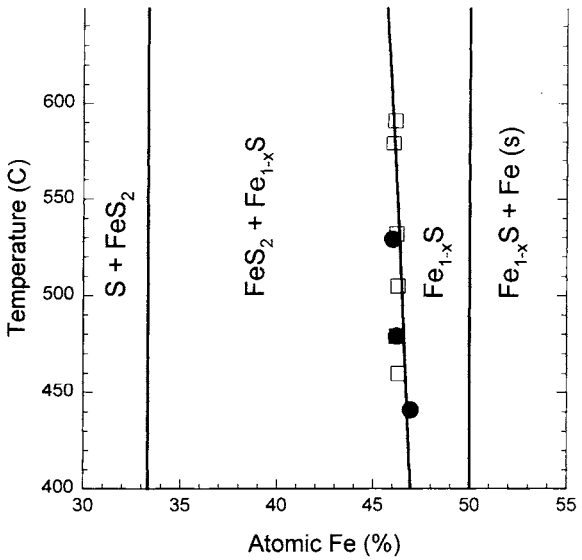

Fig. 4
The Fe-S phase diagram from 30 – 55 atomic% Fe showing the Fe content in pyrrhotite formed by pyrite thermal decomposition. Solid dots are from X-ray diffraction analyses, and the hollow squares are from electron microprobe analyses. These points are close to the solid line which is the phase boundary between the one phase pyrrhotite stability field, and the two phase pyrite + pyrrhotite stability field [27]

$$\log_{10} P_{vap}\ (\text{bar}) = 16.20(\pm 0.21) - 15700(\pm 150)/T\ . \quad (3)$$

where P_{vap} is pressure of sulfur over pyrite in bars and T is in Kelvin [28].

3.2.2 Formation of OCS

Carbonyl sulfide (OCS) was observed in the furnace exhaust when pyrite decomposition was performed in CO-bearing gas mixtures (CO-CO_2, CO-SO_2-CO_2), while condensed sulfur was not observed in the water cooled gas outlet at the top of the furnace. The observations indicate that the sulfur vapor generated by reaction (1) reacted with CO via the net chemical reaction:

$$2CO + S_2 = 2OCS \quad (4)$$

Reaction (4) was also confirmed by the following observations: 1) OCS was observed only when pyrite was heated in CO-bearing gases, and the OCS concentration in the furnace exhaust was directly proportional to the initial CO concentration in the gas mixture [29]; 2) the formation of OCS does not change the rate of pyrite decomposition, indicating that OCS formation is not from reaction of CO and pyrite, which is only a source of sulfur vapor; 3) OCS was not observed when pyrite was not present in the furnace (no sulfur source); 4) no detectable OCS was observed when pyrite was heated in gases without CO.

No detectable amount of OCS was found when a gas mixture of CO (0.50%)-SO_2 (0.50%)-CO_2 was passed through the furnace at 470 °C without pyrite in the furnace. Apparently, the formation of OCS from reaction between SO_2 and CO is kinetically inhibited [29]. However, by heating pyrite in the CO (0.50%)-SO_2 (0.50%)-CO_2 mixture, the same amount of OCS was observed as when pyrite was heated at the same temperatures in a CO (0.50%)-CO_2 gas mixture. This observation again suggests that reaction (4) is the OCS formation source and that SO_2 is not involved in OCS formation under our experimental conditions [29].

3.2.3 Formation of H_2S

Stoichiometric amounts of H_2S, corresponding to the weight loss of the solid due to the release of sulfur vapor, were observed by gas chromatography in the gaseous products when pyrite decomposition was performed in a dilute H_2S (109 ppmv)-H_2 mixture. No sulfur condensation was observed in the water cooled gas outlet at the top of the furnace, indicating that a reaction between H_2 and sulfur vapor, produced by reaction (1), has taken place:

$$2H_2 + S_2(g) = 2H_2S(g) \quad (5)$$

Pyrite destruction in H_2S-H_2 mixtures is several times faster than pyrite thermal decomposition in inert gases at a given temperature. Apparently, pyrite is also attacked by H_2,

$$(1-x)FeS_2(\text{pyrite}) + (1-2x)H_2(g) = Fe_{1-x}S(\text{pyrrhotite}) + (1-2x)H_2S(g) \quad (6)$$

which accelerates pyrite destruction. This effect was also observed by Schwab and Philinis [19].

3.3 Kinetic Results

3.3.1 Gravimetric and Geometric Measurements

The reaction extent (α) was measured by two independent methods: gravimetric and geometric.

In the gravimetric method, the fraction of pyrite reacted (α_{grav}) was calculated from the observed weight loss. The fraction of pyrite reacted was calculated from the equation:

$$\alpha_{grav} = \frac{(W_f - W_0)}{W_0} f_{St} \quad (7)$$

where W_0 and W_f are the initial and final mass of the solid, and f_{St} is a stoichiometric factor derived from the mass balance in reaction (1) which converts the mass loss of the solid to the mass of pyrite reacted. For conversion to pyrrhotite with a composition of $Fe_{0.875}S$, or Fe_7S_8,

$$f_{St} = (0.875 \times \text{MW-}FeS_2)/(0.375 \times \text{MW-}S_2) = (0.875 \times 119.979)/(0.375 \times 64.132) = 4.3649$$

where MW-FeS_2 and MW-S_2 are the molecular weights (119.979 and 64.132 g mol^{-1}).

In the geometric method, the reaction extent α_{geo} was calculated from the fractional volume change of the pyrite in the products. The equation used is,

$$\alpha_{geo} = 1 - \frac{V_f}{V_0} \tag{8}$$

where V_f and V_0 are the final and initial volume of pyrite. When the length and width of the pyrite sample are much larger than the thickness, Eq. (8) becomes:

$$\alpha_{geo} = 1 - \frac{C_f}{C_0} \tag{9}$$

where C_0 and C_f are the initial and final thickness of the pyrite. The initial thickness of the pyrite was measured with a micrometer, and the thickness of the remaining pyrite was measured with a calibrated scale by microscopic examination of cross-sections of the reacted samples.

Fig. 5 shows the generally good agreement between these two methods. An unweighted linear least square fit to the 36 points in Fig. 5 gives:

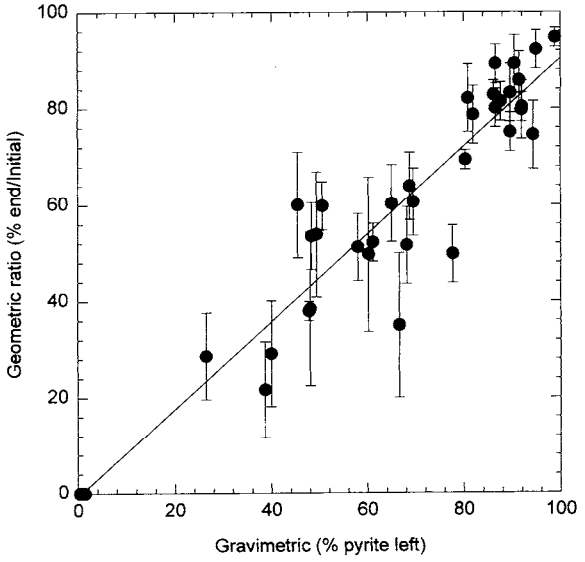

Fig. 5
Comparison of the extent of reaction (α values) obtained by the gravimetric method and the geometric method. The error bars correspond to the uncertainties in the geometric measurements. The uncertainties of the gravimetric measurements are smaller than the size of the points

$$\alpha_{geo} = 0.91 \pm 0.06\,(1\sigma)\,\alpha_{grav} - 0.006 \pm 0.09\,(1\sigma) \tag{10}$$

3.3.2 Linear Kinetics

The weight loss per surface area increases linearly with time, as shown in Fig. 6. This indicates that pyrite decomposition is a zeroth order reaction, in agreement with prior studies of pyrite decomposition in inert gases or in vacuum [10, 14, 16, 18, 22]. Linear kinetics is consistent with the optical microscopic observations which show that the product pyrrhotite layer is so porous (Fig. 3) that fresh pyrite surface is always exposed to gas flow and the gaseous product

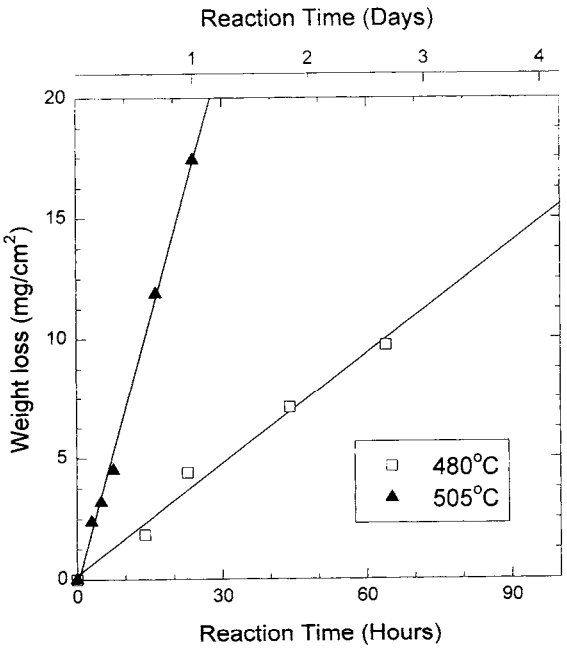

Fig. 6
Weight loss per surface area as a function of reaction time for pyrite decomposition in purified CO_2. Pyrite thermal decomposition to pyrrhotite follows linear kinetics and is not slowed down by diffusion through the porous pyrrhotite product layer

(sulfur vapor) can be easily released and escape from the solid.

The initial surface area was used in Fig. 6. During the reaction, all sides of the pyrite slice shrink constantly and the surface area becomes smaller. If the area decreases significantly, a variable surface area should be considered in Fig. 6. However, the pyrite surface area does not change significantly during most of the reaction, e.g. the surface area of a $2 \times 2 \times 0.05$ cm slice (8.40 cm^2) decreases only by 4.8% after 0.0125 cm from each of the 6 sides, or 51.2% of the pyrite, has reacted away. Our earlier studies also show that a constant surface area can be used with very little error [11, 26]. Larger error is expected as the reaction approaches completion.

3.3.3 Calculation of Rate Constant k

Once α is known and the linear kinetics behavior is established, the rate constant k of pyrite decomposition can be calculated from the equation,

$$(1-\alpha) = \frac{(a_0 - 2kt)}{a_0}\,\frac{(b_0 - 2kt)}{b_0}\,\frac{(c_0 - 2kt)}{c_0} \tag{11}$$

where a_0, b_0, c_0 are the initial length, width and thickness of the thin rectangular plates of pyrite, k is the zeroth order rate constant, and α is the reaction extent at time t. We used the α_{grav} values in Eq. (11) because these have been measured for all samples and have smaller uncertainties than the α_{geo} values. We solved Eq. (11) analytically using a computer spreadsheet [11].

Table 1
Summary of literature data for pyrite decomposition kinetics

Authors	Temp. (°C)	Experimental conditions and results
Jagadeesh and Seehra 1981 [1]	22 – 485	Magnetic susceptibility, heating-cooling curves; He, vac, H_2, CO; no rate data or E_a
Schoenlaub 1969 [2]	400 – 1000	DTA and TGA, heating-cooling curves; air, O_2, CO_2, wet and dry N_2, CO; no rate data or E_a
Hagni et al. 1992 [5]	400 – 850	Roasting in air, microscopy indicates linear kinetics, no kinetic data or E_a
Banerjee 1976 [9]	25 – 900	DTA and TGA heating curves, XRD, in air, N_2, no rate or E_a
Gallo 1927 [12]	180 – 700	Pyrite reduction in H_2, H_2O/H_2, no rate or E_a
Hedvall and Hedin 1943 [13]	596 – 820	N_2; cubic and octahedral faces decompose at different rates
Marchal 1924 [15]	500 – 1225	Vacuum, N_2
Safiullin and Gitis 1968 [17]	580 – 800	DTA and TGA heating curves; Ar, air
Thompson and Tilling 1923 [20]	350 – 1020	Isothermal weight loss; air, CO_2, CO, H_2, steam, coal gas; no rate constant or E_a
Udintseva and Chufarov 1941 [21]	400 – 750	Isothermal weight loss; vacuum, Ar; linear kinetics, 110 kJ/mol
Zhukovskii et al. 1967 [22]	450 – 690	Isothermal weight loss in N_2, vacuum, linear kinetics, 110 kJ/mol
Samal 1966 [18]	486 – 554	Isothermal weight loss; vacuum; linear kinetics, 120 kJ/mol
Schwab and Philinis 1947 [19]	400 – 650	Isothermal weight loss; air, CO_2, H_2; linear kinetics, 130 kJ/mol
Fegley et al. 1995 [11]	390 – 531	Isothermal weight loss; CO_2 and mixtures; microscopy, XRD; linear kinetics, 140 kJ/mol
Coats and Bright 1966 [10]	600 – 653	Isothermal weight loss; Ar; Arrhenius equations; linear kinetics, 281 kJ/mol
Hoare et al. 1988 [14]	427 – 927	DTA and TGA heating curves; N_2; linear kinetics, 286 kJ/mol
Pannetier and Davignon 1961 [16]	451 – 476	Isothermal weight loss; vacuum; linear kinetics, 310 kJ/mol
This work	400 – 590	Isothermal weight loss; inert, oxdizing and reducting gases; X-ray diffraction, microscopy, electron microprobe, gas chromatography; linear kinetics, 297 kJ/mol in inert gases

Two groups of activation energies (E_a) could be found: 1) four values averaging 294 ± 13 kJ/mol, and 2) five values averaging 122 ± 13 kJ/mol

Table 2
Experimental data for pyrite decomposition in helium and nitrogen

Run no.	Temperature [°C]	Time [h]	Mass loss [%]	$\log_{10}$ rate constant [cm/h]
Ultra high purity He (99.999%)				
H125	432	161.5	0.78	−4.979[a])
H138	464	66.0	1.17	−4.346[a])
H137	490	66.0	6.98	−3.641[a])
H142	522	4.2	3.08	−2.808[a])
H143	551	4.2	16.85	−2.128[a])
Ultra high purity N_2 (99.999%)				
H159	447	114	0.57	−4.945[a])
H160	471	114	2.50	−4.302[a])
H165	475	90.2	24.16	−3.512
H167	502	24	23.09	−3.077
H166	502	41	22.26	−3.022
H163	507	6.0	2.0	−3.177[a])
H162	530	6.0	12.01	−2.280[a])
H169	536	4.3	18.31	−2.199

[a]) Gas flow rate of 75 ml/min was used, rate constants are corrected to the value of 150 ml/min.

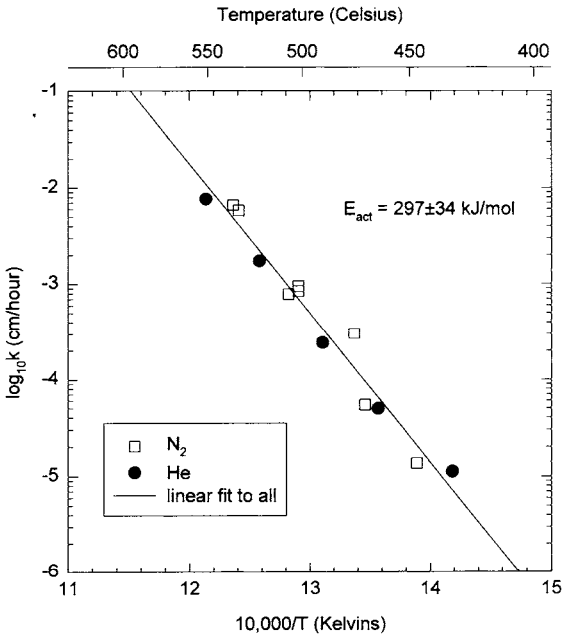

Fig. 7
Temperature dependence of the rate constant for pyrite decomposition (Arrhenius plot) in inert gases. An activation energy of 297 ± 34 (2σ) kJ/mol was derived from the slope of the linear fit

There are two special cases: 1) when $a_0 = b_0 = c_0$, Eq. (11) becomes the well-known contracting volume equation [30]

$$(1-\alpha)^{1/3} = 1 - \frac{2kt}{a_0} \tag{12}$$

2) for a thin slice where a_0 and $b_0 \gg c_0$, Eq. (11) can be simplified as Eq. (13),

$$\alpha = 2kt/c_0 \tag{13}$$

as also demonstrated by Fegley et al. [11]. This equation can be easily solved.

The experimental conditions for pyrite decomposition in various gas mixtures, and the rate constants k, calculated from Eq. (11), are summarized in Tables 2 to 7. We compared the rate constants calculated from Eqs. (11) and (13), and found that the values calculated from Eq. (13) are con-

Table 3
Experimental data for pyrite decomposition in CO_2

Run no.	Temperature [°C]	Time [h]	Mass loss [%]	$\log_{10}k$ [cm h^{-1}]
Pyrite decomposition in Coleman Instrument Grade (99.99%) CO_2				
H1	477	70.0	7.29	−3.923
H10	477	70.0	7.92	−3.891
H13	478	68.0	12.62	−3.578
H12	478	70.0	12.67	−3.686
H15a	478	69.0	10.13	−3.676
H15b	478	70.0	6.81	−3.859
H11	479	69.0	9.63	−3.790
H14a	479	70.0	7.29	−3.880
H14b	479	70.0	8.01	−3.843
H8a	480	70.0	12.17	−3.693
H8b	480	70.0	10.39	−3.769
H16a	508	38.0	18.97	−3.213
H16b	508	38.0	14.38	−3.230
H17a	530	11.0	20.02	−2.562
H17b	530	11.0	22.58	−2.510
H18a	530	11.0	18.69	−2.568
H18b	530	11.0	17.38	−2.617
Pyrite decomposition in Coleman grade CO_2 with O_2 purifiers				
H28a	465	64.0	3.08	−4.197
H28b	465	64.0	1.83	−4.464
H25a	509	20.0	11.32	−3.099
H25b	509	20.0	12.25	−3.108
H26	529	5.1	11.84	−2.466
Pyrite decomposition in Coleman grade CO_2 with O_2 and H_2O purifiers				
H36	460	109.0	4.14	−4.273
H75	460	161.5	13.75	−4.029
H58	479	44.0	7.12	−3.652
H53	480	14.0	1.84	−3.781
H50	480	22.8	4.39	−3.554
H68	481	64.0	9.72	−3.742
H54	505	3.0	2.38	−3.089
H64	505	5.0	3.17	−3.040
H66	505	7.5	4.50	−3.059
H63	505	16.3	11.89	−3.061
H73	505	24.0	12.87	−3.161
H60	532	3.0	7.15	−2.467
H87	579	17 m[a])	7.01	−1.523
H86	591	22 m[a])	12.10	−1.339

[a]) Time in min.

sistently about 1 − 5% larger than those calculated from Eq. (11). This small difference was also noted by Fegley et al. [11], and it arises because the thickness is a few % of the length and width of the pyrite slices used in the reactions. The temperature dependence of the rate constants in different gas mixtures are plotted in Figs. 7 − 12.

Table 4
Experimental data for pyrite decomposition in CO-CO_2 gas mixtures

Run no.	Temperature [°C]	Time [h]	Mass loss [%]	$\log_{10}k$ [cm h^{-1}]
54 ppm CO in Coleman CO_2 with O_2 and H_2O purifiers				
H104	501	5.0	1.29	−3.476
H109	530	2.0	6.58	−2.345
H85	531	4.0	10.41	−2.579
H84	590	22 m[a])	15.6	−1.284
108 ppm CO in Coleman CO_2 with O_2 and H_2O purifiers				
H78	467	67.5	4.19	−4.118
H111	500	11.5	5.11	−3.227
H112	567	22 m[a])	5.25	−1.726
1003 ppm CO in Coleman CO_2 with O_2 and H_2O purifiers				
H91	447	145.0	2.83	−4.613
H102	504	15.0	11.96	−3.086
H101	591	2.2	19.47	−1.311

[a]) Time in min.

Table 5
Experimental data for pyrite decomposition in SO_2-CO_2 and SO_2-CO-CO_2 gas mixtures

Run no.	Temperature [°C]	Time [h]	Mass loss [%]	$\log_{10}k$ [cm h^{-1}]
0.96% SO_2 in Coleman CO_2 with O_2 and H_2O purifiers				
H96	436	54.0	0.65	−4.676
H77	467	22.0	1.54	−4.029
H80	500	16.5	11.29	−3.169
H81	531	4.0	9.12	−2.554
54 ppm CO, 0.48% SO_2 in Coleman CO_2 with O_2 and H_2O purifiers				
H72	469	24.0	1.83	−3.997
H71	500	14.0	7.98	−3.173
H70	530	4.0	11.59	−2.450
H74	570	1.0	10.9	−1.853
H82	589	22 m[a])	12.5	−1.306

[a]) Time in min.

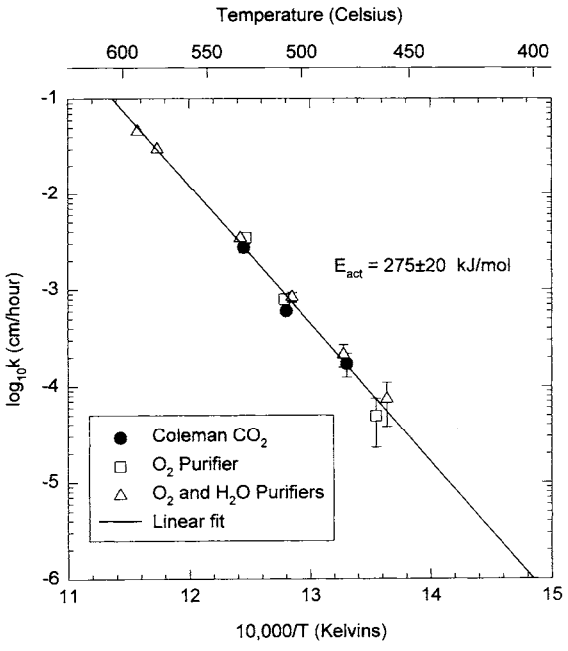

Fig. 8
Arrhenius plot for pyrite decomposition in CO_2 with and without removal of trace H_2O and/or O_2 impurities found in Coleman grade CO_2 (99.99%). The activation energy and rate constants for pyrite decomposition are not appreciably changed by the impurities. The error bars correspond to the range of rate constants measured in different runs at the same temperature

3.4 Effect of Gas Composition on Pyrite Decomposition

The gas mixtures used in the pyrite decomposition experiments can be divided into three categories: inert, oxidizing, and reducing.

Table 6
Experimental data for pyrite decomposition in an O_2-CO_2 gas mixture

Run no.	Temperature [°C]	Time [h]	Mass loss [%]	$\log_{10}k$ [cm h^{-1}]
100 ppm O_2 in Coleman CO_2 with H_2O purifiers				
H99[a])	392	166	9.24	−4.430
H92[a])	430	144	13.04	−4.056
H89[a])	460	47.2	5.83	−3.839
H124	484	18.0	3.35	−3.561
H116	503	14.2	13.22	−3.061
H127	522	3.17	6.71	−2.713
H123	538	3.00	22.81	−2.163
1009 ppm O_2 in Coleman CO_2 with H_2O purifiers				
H129[a])	414	94.0	5.37	−4.246
H128[a])	433	70.5	25.11	−3.561
H130[a])	435	7.50	4.32	−3.244
H135[a])	436	15.5	8.24	−3.398
H131[a])	466	10.5	8.42	−3.089
H136[a])	500	15.5	33.01	−2.631
H132	508	10.5	13.22	−2.720
H134	543	4.40	15.46	−2.303
H133	560	0.50	7.65	−1.755

[a]) XRD also shows hematite, in addition to pyrrhotite, in the run products.

Table 7
Experimental data for pyrite decomposition in a H_2S-H_2 gas mixture

Run no.	Temperature [°C]	Time [h]	Mass loss [%]	$\log_{10}k$ [cm h^{-1}]
109 ppm H_2S in ultra high purity H_2 (99.999%)				
H94	397	43.5	2.81	−4.158
H90	400	51.7	1.72	−4.409
H98	416	15.2	1.15	−4.119
H107	441	16.4	3.28	−3.622
H103	458	15.2	5.31	−3.275
H108	460	16.4	8.01	−3.173
H105	480	4.1	4.43	−2.798
H106	502	4.1	8.90	−2.493

3.4.1 *Pyrite Decomposition in Inert Gases and CO_2-Bearing Gases*

The temperature dependent rate constants for pyrite decomposition in He and N_2, CO_2, CO-CO_2, and SO_2-CO-CO_2 are plotted in Figs. 7 – 10. As shown in Table 8, the rate constants are practically the same at a given temperature. Only pyrrhotite with slightly different Fe/S ratios and residual pyrite were observed in the products. Pyrite decomposition in these gases and gas mixtures can be therefore considered as pure pyrite thermal decomposition via Eq. (1).

The apparent activation energy for pyrite decomposition in He and N_2 is $297 \pm 34 (2\sigma)$ kJ/mol (Fig. 7). In CO_2, and in CO-CO_2 or CO-SO_2-CO_2 gas mixtures, the apparent activation energies are in the range of 260 to 275 kJ/mol, and are the same ($275 \pm 20 (2\sigma)$ kJ/mol) within experimental uncertainties.

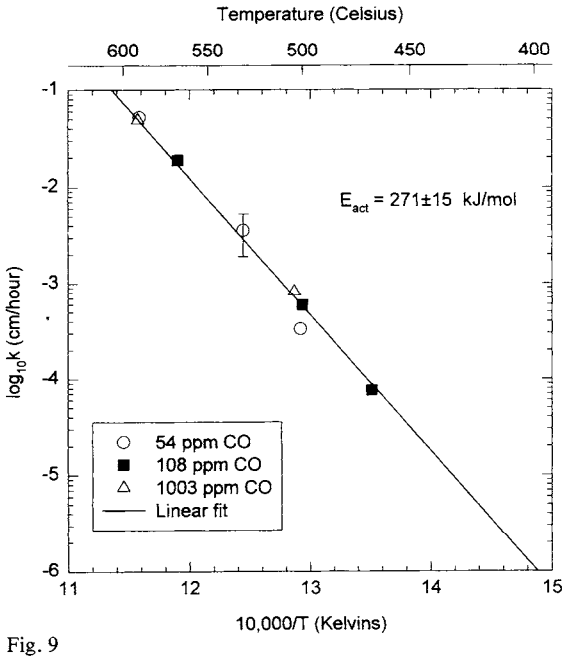

Fig. 9
Arrhenius plot of pyrite decomposition for CO-CO_2 mixtures showing that at low levels (≤0.1%), the concentration of CO does not change the rate constant of pyrite decomposition under our experimental conditions

Table 8
Rate data for pyrite decomposition in different gas mixtures

Gas mixture	Temperature range [°C]	$k = k_0 \exp(-E_a/RT)$		k at 477 °C [10^{-4} cm/h]
		$\log k_0$	E_a/kJ mol^{-1}	
He and N_2	399 – 551	16.87 ± 0.16	297 ± 34	1.5 ± 0.9
Coleman CO_2 or pure CO_2	460 – 591	15.34 ± 0.13	275 ± 20	1.5 ± 0.5
CO/CO_2	447 – 591	15.08 ± 0.13	271 ± 15	1.6 ± 0.4
SO_2/CO_2 or $CO/SO_2/CO_2$	436 – 589	14.32 ± 0.09	260 ± 22	1.6 ± 0.6
1009 ppm O_2/CO_2[a])	414 – 500	1.99 ± 0.02	82 ± 9	1.9 ± 0.3
1009 ppm O_2/CO_2	508 – 560	16.66 ± 0.18	293 ± 52	1.8 ± 1.3
109 ppm H_2S/H_2	399 – 502	9.75 ± 0.10	181 ± 10	13.9 ± 2.5

[a]) Hematite was detected in the run products, in addition to pyrrhotite.

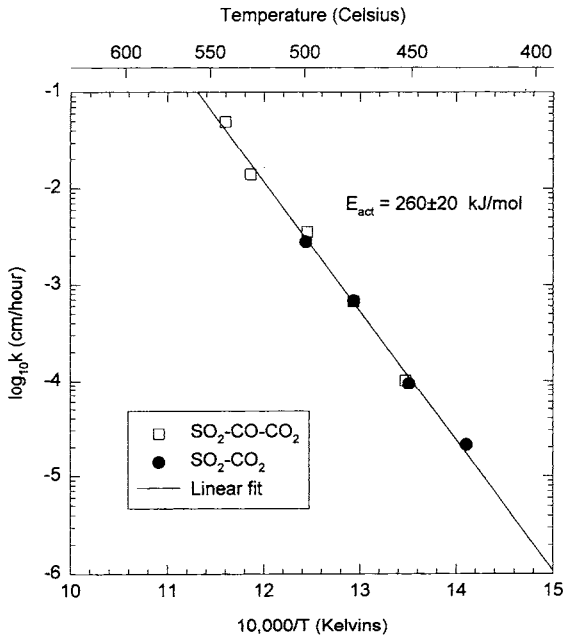

Fig. 10
Arrhenius plot of pyrite decomposition in SO_2-CO-CO_2 gas mixtures. The rate constants and activation energy are the same with or without CO in the mixture, and within error are the same as in CO_2

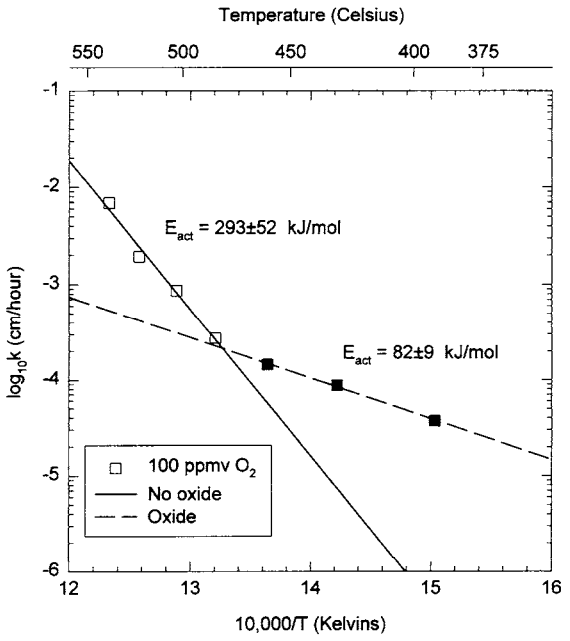

Fig. 11
Arrhenius plot of pyrite decomposition in a 100 ppmv O_2-CO_2 mixtures. Two different types of behavior are observed. At higher temperatures the reaction rates and activation energy (293 ± 52 kJ/mol) are similar to those in inert gases. At lower temperatures, XRD shows that hematite was produced, the reaction rates are faster than in CO_2, and the activation energy is lower (82 ± 9 kJ/mol)

3.4.2 *Pyrite Decomposition in Oxidizing Gases*

The experimental data for pyrite decomposition in 100 and 1009 ppmv O_2-CO_2 mixtures are listed in Table 6, and the temperature dependence of rate constants is shown in

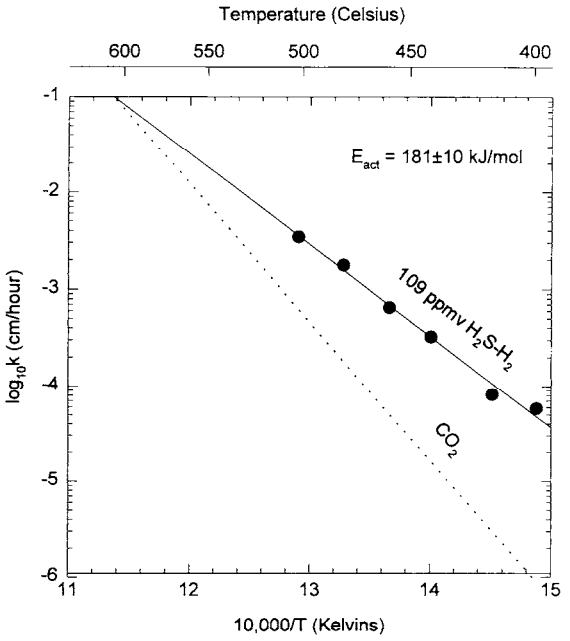

Fig. 12
Arrhenius plot of pyrite decomposition in a 109 ppmv H_2S-H_2 mixture, and comparison to pyrite decomposition in CO_2. The overall pyrite destruction can be divided into two processes (reaction (1) and (6)). The contribution of pure pyrite decomposition (reaction (1)) increases with temperature

Fig. 11. In the 100 ppmv O_2-CO_2 gas mixture, there are two different types of behavior. At higher temperatures (484 to 538 °C), no detectable hematite was observed in the products, and the rate constants are about the same as the rate constants in inert gases at a given temperature in this temperature range. The activation energy is 293 ± 52 (2σ) kJ/mol, the same as the activation energy for pyrite decomposition in inert gases. The rate constants in 1009 ppmv O_2-CO_2 mixture (listed in Table 6 but not shown in Fig. 11) with no detectable hematite in the product (508 – 560 °C) fit nicely on this regression line.

At lower temperatures (392 – 460 °C in 100 ppmv O_2-CO_2), hematite (Fe_2O_3) and pyrrhotite were observed in the products, and the rate constants are appreciably higher than those extrapolated from higher temperatures. Apparently, pyrite oxidation is taking place, via the net reaction:

$$4FeS_2 + 11O_2 = 2Fe_2O_3 + 8SO_2 \quad (14)$$

The apparent activation energy in the low temperature range is 82 ± 9 (2σ) kJ/mol in 100 ppmv O_2-CO_2. Three data points (435 – 500 °C) with hematite formation in 1009 ppmv O_2-CO_2 are not on the low temperature regression line, suggesting that the increase in oxygen fugacity changes the contributions of different reactions in the overall process. The absence of hematite at high temperatures is most likely due to a kinetic effect, because thermodynamic calculations show that hematite is stable at these temperatures even at much lower oxygen fugacity [31] and because

the hematite formation rate is much smaller than pyrrhotite formation rate.

The pyrite decomposition product, pyrrhotite, may also react with O_2 to form hematite:

$$2Fe_{1-x}S + (3.5 - 1.5x)O_2 = (1-x)Fe_2O_3 + 2SO_2 \quad (15)$$

However, as long as pyrrhotite is present in the solid, reaction (15) will not alter the overall pyrite decomposition rate, and only reaction (14) will accelerate the rate of pyrite destruction.

3.4.3 Pyrite Decomposition in Reducing Gases

In the 109 ppmv H_2S-H_2 gas mixture, the rate constants for pyrite destruction are several times faster than the rate constants for pyrite thermal decomposition in inert gases (see Fig. 12). Gas chromatography shows that the H_2S concentrations in the gaseous products are much larger than the initial 109 ppmv, so the initial H_2S in the mixture does not seem to have a significant effect on the overall process.

Pyrite destruction in H_2S-H_2 gas mixtures probably consists of two chemical reactions: thermal decomposition, as shown in reaction (1), and destruction of pyrite by H_2, as shown in reaction (6). The increase in the rate constant for pyrite destruction in H_2 mixtures, with respect to that in inert gases, is apparently due to reaction (6). However, the effect is smaller as the reaction temperature is increased, which suggests that the activation energy for reaction (6) is less than that for reaction (1). Indeed, Schwab and Philinis [19] reported an activation energy of ~ 120 kJ/mol for reaction (6). Our activation energy of $181 \pm 10(2\sigma)$ kJ/mol is for the overall process.

4. Discussion

4.1 Literature Data and Thermodynamic Calculations

4.1.1 Enthalpy of Reaction

In an endothermic solid decomposition, the activation energy is normally approximately equal to or slightly higher than the overall enthalpy change of the reaction, if the reactants and the products are both in their standard states [32].

The enthalpy change for pyrite thermal decomposition (Eq. (1)), was calculated for two extreme cases: reaction (16), which produces troilite (FeS) and reaction (17) which produces low-Fe pyrrhotite (Fe_7S_8):

$$2FeS_2 \text{ (pyrite)} = 2FeS + S_2 \text{ (gas)} \quad (16)$$

$$7/3\,FeS_2 \text{ (pyrite)} = 8/3\,Fe_{0.875}S \text{ (pyrrhotite)} + S_2 \quad (17)$$

Reactions (16) and (17) were used because FeS and Fe_7S_8 are at Fe-rich and Fe-poor ends of the pyrrhotite stability field in the Fe-S phase diagram.

We used updated thermodynamic data [33] to calculate the enthalpy change for pyrite decomposition in the temperature range of 600 – 900 K (327 – 627 °C), which spans the temperature range in our experiments. The enthalpy change for reaction (16) is 284.7 ± 0.3 kJ per mole of S_2 vapor, and that for reaction (17) is 285.2 ± 3.2 kJ per mole of S_2 vapor. They are the same within the uncertainty of the thermodynamic data.

There are several thermodynamic equilibrium measurements of the sulfur vapor pressure over pyrite in the literature [34 – 43], and the experimental conditions and the enthalpy changes are summarized in Table 9. The enthalpy changes in Table 9 may be divided into two groups: 1) around 295 ± 20 kJ/mol, which agrees with the calculated value, and 2) 415 ± 39 kJ/mol, which is appreciably larger than the calculated value of the enthalpy change for reaction (16) or (17).

The high enthalpy values observed by the Dickson et al. [35], Raeder [38], and Allen and Lombard [42], are probably due to the change in molecular speciation (S, S_2, S_3, ... S_8) of sulfur vapor under their experimental conditions. Their temperature ranges are generally high, e.g. 647 to 681 °C [35], 590 – 686 °C [38], and 575 – 680 °C [42]. In general, higher temperature will decrease the fractions of the heavier allotropes (S_8, S_7, S_6, ...) and larger sulfur vapor pressure will increase the fraction of the heavier allotropes. Under our experimental conditions, S_2 is the dominant allotrope [28], and reaction (17) represents the real vaporization process. At higher temperatures, the sulfur vapor pressure over pyrite increases exponentially, and the fraction of heavier sulfur allotropes is not negligible. Thermodynamic calculations for reaction such as:

$$4FeS_2 = 4FeS + S_4 \quad \Delta H^0_{vap} = 460.6 \pm 0.3 \quad (18)$$

$$6FeS_2 = 6FeS + S_6 \quad \Delta H^0_{vap} = 578.1 \pm 2.8 \quad (19)$$

$$8FeS_2 = 8FeS + S_8 \quad \Delta H^0_{vap} = 737.8 \pm 4.6 \quad (20)$$

show that the vaporization enthalpy of heavier sulfur allotropes is larger than that of S_2 (data for S_x from JANAF [44]). Thus, the overall enthalpy change for pyrite thermal decomposition increases with increasing temperature due to the contribution of heavier sulfur allotropes, and the real vaporization process is to a vapor with substantial amounts of heavier allotropes (S_3 ... S_8).

In the temperature range between 388.36 – 882.1 K (115.21 – 608.9 °C), liquid sulfur is the most stable state of sulfur [33]. It is plausible to divide the overall process for reaction (16) into two steps: 1) decomposition of pyrite to pyrrhotite and liquid sulfur (reaction 21), and 2) vaporization of liquid sulfur to sulfur gas (reaction 22).

$$2FeS_2 \text{ (pyrite)} = 2FeS + 2S \text{ (liq)} \quad (21)$$

$$2S \text{ (liq)} = S_2 \text{ (gas)} \quad (22)$$

Similar steps (reactions (23) and (22)) may be proposed for reaction (17).

$$7/3\ FeS_2 \text{ (pyrite)} = 8/3\,Fe_{0.875}S \text{ (pyrrhotite)} + 2S \text{ (liq)} \quad (23)$$

Table 9
Literature data for the sulfur vapor pressure over pyrite and pyrrhotite, ΔH^0_{vap} was calculated from the slope of $\log_{10}(P_{vap})$ vs. $10000/T$

Authors and references	T [°C]	Method	ΔH^0_{vap} (kJ/mol)
Dickson et al. 1962 [35]	647 – 681	Manometry	449
Allen and Lombard 1917 [42]	575 – 680	Dew point	412
Raeder 1929 [38]	590 – 686	Manometry	383
de Rudder 1936 [34]	600 – 690	Manometry	327
Toulmin and Barton 1964 [41]	324 – 743	Electrum tarnish	304
Bog and Rosenquist 1959 [43]	500 – 552	Manometry	301
Hong and Fegley 1997 [28]	436 – 591	Transpiration	297
Schneeberg 1973 [40]	324 – 438	Sulfur vapor sensor	292
Rau 1976 [39]	547 – 743	Manometry	276
D'Or 1931 [36]	548 – 676	Manometry	266
Giletti et al. 1968 [37][a])	420 – 600	Radioactive S isotopes	234

[a]) Not considered because of experimental difficulties.

$$2S\ (liq) = S_2\ (gas) \quad (22)$$

We calculate the enthalpy changes for reactions (21) and (23), as 173.1 ± 3.2 kJ/mol and 174.2 ± 3.5 kJ/mol respectively, which are the same within the uncertainties of the thermodynamic data. The enthalpy change of reaction (22) is 111.6 ± 3.5 kJ/mol in the range of 600 – 800 K.

4.1.2 Activation Energy

The activation energy values listed in Table 1 can be roughly divided into two groups: 1) four values averaging 294 ± 13 kJ/mol, and 2) five values averaging 122 ± 13 kJ/mol. The two groups of apparent activation energy values indicate different rate-limiting steps for pyrite decomposition. The higher activation energy values of about 294 kJ/mol suggest that pyrite decomposition to pyrrhotite and sulfur vapor (reaction (17), where $\Delta H^0_{vap} \sim 285$ kJ/mol) is the rate-limiting step, and the lower activation energy values of about 122 kJ/mol suggest that the vaporization of sulfur is the rate-limiting step (reaction (22), where $\Delta H^0_{vap} \sim 112$ kJ/mol).

Such a transition in the apparent activation energy may result from different experimental conditions. Suppose pyrite decomposition is done in a gas flow system. Pyrite decomposition (reaction (17)) can be divided into two steps (reactions (21) and (22)). If the flow rate is very low, the sulfur vapor (dominantly S_2) will be swept away very slowly, and the vaporization of sulfur may become the rate-limiting step in pyrite decomposition. Thus the apparent activation energy for the overall process will be close to the enthalpy change of reaction (22) (~ 112 kJ/mol). However, if the gas flow rate is high enough to rapidly sweep away the sulfur formed from pyrite decomposition, the activation energy will be close to the overall enthalpy change (~ 285 kJ/mol), which is the enthalpy change of pyrite decomposition to pyrrhotite and sulfur vapor (S_2).

4.2 Mechanism of Pyrite Decomposition

Pyrite decomposition may be divided into two steps: 1) decomposition of pyrite to pyrrhotite and liquid sulfur, and 2) evaporation of liquid sulfur to sulfur gas (S_2). It could be simplified as the reaction sequence of (23) and (22).

The mechanism of pyrite thermal decomposition apparently depends on the experimental conditions. If the vaporization of liquid sulfur is fast enough, the overall process will be close to one-step release of a S_2 molecule from two nearby FeS_2 molecules, which can be simplified by reaction (16) and was illustrated by Fegley et al. [11]. The apparent activation energy will be close to the enthalpy change of ~ 285 kJ/mol for reaction (17). If the vaporization is not fast enough, and the rate of the overall process is limited by this step, then the apparent activation energy will be close to the enthalpy change of ~ 112 kJ/mol for reaction (19).

5. Summary

We studied pyrite thermal decomposition at ambient pressure in flowing He, N_2, CO_2, CO_2-CO-SO_2, O_2-CO_2 and H_2S-H_2 gas mixtures from 400 – 590 °C using optical microscopy, X-ray diffraction, electron microprobe analyses, and gas chromatography. Pyrite decomposition to pyrrhotite ($Fe_{1-x}S$) and sulfur vapor (S_2) was observed in all gases and follows linear kinetics. The composition of the pyrrhotite product follows the phase boundary between the one phase pyrrhotite stability field and the two phase pyrite + pyrrhotite stability field in the Fe-S phase diagram. The rate constants were measured from the weight loss of the reacted samples and the thickness change of residual pyrite in reacted samples. The apparent activation energy for pyrite thermal decomposition to pyrrhotite is $297 \pm 34(2\sigma)$ kJ mol^{-1} in inert gases (He, N_2). In CO_2 and low concentration CO-SO_2 mixtures with CO_2, the activation energy of $275 \pm 20(2\sigma)$ kJ mol^{-1} is similar to that in inert gases and the rate constants are the same as in inert gases at a given temperature. In oxidizing (O_2-CO_2) or reducing (H_2S-H_2) gas mixtures, the rate constants are larger than that of pure thermal decomposition because additional reactions between pyrite and oxidizing/reducing gases accelerate pyrite decomposition, and reduce the ap-

parent activation energy. Pyrite decomposition may be divided into two processes: 1) formation of pyrrhotite and liquid sulfur, 2) vaporization of liquid sulfur. This mechanism explains the discordant data of the enthalpy change and the activation energy of pyrite thermal decomposition in the literature.

This work was supported by Grant NAG5-4564 from NASA Planetary Atmospheres Program. We thank K. Lodders, M.Yu. Zolotov and D. Lauretta for helpful discussions. We also thank D. Kremser, and R. Poli for their technical support and an anonymous referee for careful reviewing.

References

[1] M.S. Jagadeesh and M.S. Seehra, J. Phys. D *14*, 2153 (1981).
[2] R.A. Schoenlaub, J. Am. Ceram. Soc. *52*, 40 (1969).
[3] G. Martin and J.L. Foucar, Sulfuric Acid and Sulfur Products, Crosby Lockwood and Son, London, 1916.
[4] A.M. Fairlies, Sulfuric Acid Manufacture, ACS Monograph Series, Reinhold Publishing, Company, New York, 1936.
[5] A.M. Hagni, R.D. Hagni, and P.R. Taylor, EPD Congress 1993, 393 (1992).
[6] D.J. Vaughan and J.R. Craig, Mineral Chemistry of Metal Sulfides, Cambridge University Press, Cambridge, 1978.
[7] U. Von Zahn, S. Kumar, H. Niemann, and R.G. Prinn, Composition of the Venus Atmosphere, in: Venus, ed. by D.M. Hunten, L. Colin, T.M. Donahue, and V.I. Moroz, University of Arizona Press, Tucson, 1983.
[8] J.S. Lewis, Icarus *50*, 103 (1982).
[9] A.C. Banerjee, Indian J. Chem. *14A*, 845 (1976).
[10] A.W. Coats and N.F.H. Bright, Can. J. Chem. *44*, 1191 (1966).
[11] B. Fegley Jr., K. Lodders, A.H. Treiman, and G. Klingelhöfer, Icarus *115*, 159 (1995).
[12] G. Gallo Ann. Chim. Appl. *17*, 39 (1927).
[13] J.A. Hedvall and R. Hedin, Die Chemie *56*, 45 (1943).
[14] I.C. Hoare, H.J. Hurst, W.I. Stuart, and T.J. White, J. Chem. Soc. Faraday Trans. I *84*, 3071 (1988).
[15] G. Marchal, Bull. Soc. Chim. *35*, 43 (1924).
[16] G. Pannetier and L. Davignon, Bull. Soc. Chim. *72*, 1513 (1961).
[17] N.Sh. Safiullin and E.B. Gitis, J. Appl. Chem. USSR *41*, 1596 (1968).
[18] G.I. Samal, Geterogennye Khim. Reaktsii, Inst. Obshch. i Neorgan. Khim. Akad. Nauk Belorussk. SSR 93 (1965).
[19] G.M. Schwab and J. Philinis, J. Am. Chem. Soc. *69*, 2588 (1947).
[20] F.C. Thompson and N. Tilling, J. Soc. Chem. Ind. XLIII, 37T (1924).
[21] V.S. Udintseva and G.I. Chuforov, J. Appl. Chem. USSR *14*, 3 (1941).
[22] V.M. Zhukovskii, I.A. Montilo, and A.A. Babadzhan, Tr. Ural. Nauch. Issled. Proekt. Inst. Med. Prom. *8*, 387 (1965).
[23] W.A. Deer, R.A. Howie, and J. Zussman, Rock-Forming Minerals, Vol. 5, J. Wiley and Sons, New York, 1963.
[24] B. Fegley Jr. and R.G. Prinn, Nature *337*, 55 (1989).
[25] R.A. Yund and H.T. Hall Econ. Geol. *64*, 420 (1969).
[26] D.S. Lauretta, D.T. Kremser, and B. Fegley Jr., Icarus *122*, 288 (1996).
[27] S.J. Stolen and F. Gronvold, J. Phys. Chem. Solids *48*, 1213 (1987).
[28] Y. Hong and B. Fegley Jr., Planetary Space Sci. (1997) in press.
[29] Y. Hong and B. Fegley Jr., Icarus, (1997) in press.
[30] M.E. Brown, D. Dollimore, and A.K. Galwey, Theory of solid state reaction kinetics, in: Comprehensive Chemical Kinetics, ed. by C.H. Bamford and C.F.H. Tipper, Vol. 22, pp. 41 – 113, Elsevier, Amsterdam, 1980.
[31] B. Fegley Jr., Icarus, *128*, 474 (1997).
[32] D.A. Young, Solid and Surface Kinetics, in: The International Encyclopedia of Physical Chemistry and Chemical Physics, Topic 21, Vol. 1, ed. by F.C. Tompkins, Pergamon Press, 1966.
[33] R.A. Robie and B.S. Hemingway, U.S. Geological Survey Bulletin 2131, United States Government printing Office, Washington D.C., 1995.
[34] M.F. deRudder, Bull. Soc. Chim. France *47*, 1225 (1936).
[35] F.W. Dickson, L.D. Shields, and G.C. Kennedy, Econ. Geol. *57*, 1021 (1962).
[36] L. D'Or, J. Chim. Phys. *28*, 337 (1931).
[37] B.J. Giletti, R.A. Yund, and T.H. Lin, Econ. Geol. *63*, 702 (1968).
[38] M.G. Raeder, Kgl. Norske Videnskabers Selskab, *II(43)*, 151 (1929).
[39] H. Rau, J. Phys. Chem. Solids *37*, 425 (1976).
[40] E.P. Schneeberg, Econ. Geol. *68*, 507 (1973).
[41] P. Toulmin III and P.B. Barton Jr., Geochim. Cosmochim. Acta *28*, 641 (1964).
[42] E.T. Allen and R.H. Lombard, Am. J. Sci. *43*, 175 (1917).
[43] S. Bog and T. Rosenqvist, Trans. Faraday Soc. *55*, 1565 (1959).
[44] M.W. Chase Jr., C.A. Davis, J.R. Downey Jr., D.J. Frurip, R.A. McDonald, and A.N. Syverrud, JANAF Thermochemical Tables, 3rd ed., J. Phys. Chem. Ref. Data *14* (Suppl. 1), Am. Chem. Soc. and Am. Inst. of Phys. (1985).

(Received: September 2, 1997) E 9595